7
The G-band and Time-Independent Perturbations

With the materials science and Raman spectroscopy background now in place in Chapters 1–6, we are now ready to start analyzing the Raman spectra of nanocarbons. In the next two chapters we discuss detailed aspects of the Raman G-band (where the notation G comes from graphite). In order to understand the G-band spectra in detail, we have to study the origin of the perturbations to the G-band, caused first by time-independent perturbations, such as strain, which are considered in this chapter, and second by time-dependent perturbations, such as the electron–phonon coupling, which is considered in Chapter 8, where we discuss the effect of temperature and gate voltage on the G-band spectra.

The G-band has two basic properties which make it special for studying sp^2 materials:

- The G-band is present in the Raman spectra of all sp^2 carbon systems, at around $1580\,\mathrm{cm}^{-1}$. It is related to the in-plane C–C bond stretching mode, which gives rise to both the optical in-plane transverse optic (iTO) phonon and the longitudinal optical (LO) phonon branches in graphitic materials.
- Due to the strong C–C bonding and small mass of the C atoms, the G-band in sp^2 carbons has a relatively high Raman frequency in comparison to other materials, and very small perturbations to ω_{G} can be measured.

Since the carbon atoms in sp^2 carbon materials are neutral (neither positively nor negatively charged), both the iTO phonon and the LO phonon have the same frequency at the zone center of the Brillouin zone.[1)] Although the iTO and LO phonon modes are degenerate at the Γ point in both graphite and graphene and are known to comprise the Γ_3^+ doubly degenerate symmetry phonon modes (E_{2g} in point group notation, see Section 6.3.4),[2)] only the LO phonon mode has a large Raman intensity. However, in the presence of strain, such as occurs in carbon nanotubes, the LO and iTO phonon modes are mixed with each other, so that both phonon

1) In an ionic crystal, the LO phonon has a higher frequency than the TO phonon mode since the Coulomb interaction acts only on the LO mode.
2) Since there is another E_{2g} symmetry mode in the acoustic phonon branch, we sometimes denote the degenerate iTO and LO optical mode as the $E_{2g}(2)$ or E_{2g2} mode, while the degenerate acoustic mode is denoted by the $E_{2g}(1)$ or E_{2g1} mode.

Raman Spectroscopy in Graphene Related Systems. Ado Jorio, Riichiro Saito, Gene Dresselhaus, and Mildred S. Dresselhaus

ISBN: 978-3-527-40811-5

modes become Raman-active. The iTO and LO phonon frequencies are split into two peaks, and the splitting between the peaks is increased by increasing the strain.

Usually it is hard to observe the splitting of two phonon modes in a material by hydrostatic pressure or by uniaxial strain. However, in the case of the G-band, which has a high-frequency, it becomes possible to observe a clear strain-induced splitting. In fact, while a 1% strain-induced change to a $100\,\mathrm{cm}^{-1}$ Raman feature lies within the $\pm 1\,\mathrm{cm}^{-1}$ precision of most experimental set-ups, a 1% change in the G-band frequency corresponds to $\sim 16\,\mathrm{cm}^{-1}$, which is larger than the natural width of $\sim 10\,\mathrm{cm}^{-1}$ for the G-band features.[3] For this reason, small changes in the physical properties due to strain, as is produced by rolling up the graphene sheet in forming a carbon nanotube, introduce easily measurable strain-induced changes in the G-band feature.

In this chapter we review the detailed G-band properties as a function of strain, which splits the iTO and LO frequencies in graphene (Section 7.1) and carbon nanotubes (Section 7.2). For carbon nanotubes we also consider the effect of quantum confinement (Section 7.3), which is important in both carbon nanotubes and nanoribbons, although the latter will not be treated here.

7.1
G-band in Graphene: Double Degeneracy and Strain

The graphene hexagonal lattice is isotropic in two dimensions. The elastic tensor in graphene is isomorphic to the elastic tensor of the two-dimensional full rotation symmetry group, and this is why nowadays the soccer net is based on hexagonal lattice symmetry.[4] As a result of this symmetry, the LO and iTO phonon modes of graphene are degenerate at the Γ point. This degeneracy is broken when moving away from the Γ point in the Brillouin zone, since the introduction of a phase-directional spatial modulation breaks the rotational symmetry. As a result, the concepts of longitudinal (L) and in-plane transverse (iT) optical (O) modes[5] are expressed with respect to the modulation direction along which the strain is applied.

3) The natural width of a Raman spectral feature is given by the lifetime of the phonons. This will be discussed further in Chapter 8.

4) The hexagonal net was selected for the 1990 world cup in Italy. A hexagonal net produces the shortest length of strings per a unit area and is more flexible and more isotropic than a stiff and anisotropic square net. Since a 120° angle in the hexagonal net is used for the soccer goal, the net can be expanded up to 180°, and the soccer ball can go deeper into the goal net. The shock wave on the net propagates isotropically from the ball, and the ball can be seen to stop clearly at the goal point. The animation can be seen in the following web site: http://www1.gifu-u.ac.jp/~eng/ja/square/2004syou/exciting/exciting.htm.

5) In the transverse mode for two-dimensional materials, we have in-plane and out-of-plane TO modes, while the longitudinal mode is always an in-plane mode. Thus we do not say iLO, but rather we simply say LO for the longitudinal mode.

7.1.1 Strain Dependence of the G-band

When the bond lengths and angles of graphene are modified by strain, the hexagonal symmetry of graphene is broken, and this symmetry-breaking effect splits the LO and iTO mode frequencies [198, 230, 231]. The understanding of this effect comes from elasticity theory [95], which is discussed in many textbooks on the introduction to solid state physics. The dynamic equation for the deformation of the lattice within the linear displacement regime is given by the equations of motion [232]:

$$-M\ddot{u}_i = M\omega_0^2 u_i + \sum_{klm} K_{iklm}\epsilon_{lm}u_k \ , \quad (i,m,k,l=1,2) \ , \tag{7.1}$$

where $u_i (i = 1, 2)$ is the in-plane atomic displacement, M is the mass of the carbon atom, and ω_0 is the frequency for the unstrained lattice. Here ϵ_{lm} denotes the strain tensor in the in-plane coordinates which can be obtained by rotating the strain tensor[6] in the phonon propagating direction ℓ (longitudinal) and in its perpendicular direction t (transverse), as $\epsilon_{\ell\ell}$ and ϵ_{tt}. The subscripts ℓ and the t denote, respectively, the in-plane directions of the vibration of the LO and iTO phonon modes [232], so that we can write the strain tensor for u_1 and u_2 as:

$$\begin{pmatrix} \epsilon_{11} & \epsilon_{12} \\ \epsilon_{21} & \epsilon_{22} \end{pmatrix} = \begin{pmatrix} \epsilon_{tt}\cos^2\theta + \epsilon_{\ell\ell}\sin^2\theta & \sin\theta\cos\theta\,(\epsilon_{\ell\ell} - \epsilon_{tt}) \\ \sin\theta\cos\theta\,(\epsilon_{\ell\ell} - \epsilon_{tt}) & \epsilon_{tt}\sin^2\theta + \epsilon_{\ell\ell}\cos^2\theta \end{pmatrix} \ , \tag{7.2}$$

where the angle θ denotes the angle between u_1 and the iTO (u_2 and LO) phonon direction.

The fourth rank tensor K_{iklm} gives the change in the elastic constant K_{ik} between the displacements u_i and u_k due to ϵ_{lm}, which is defined as:[7]

$$K_{iklm} = \frac{\partial K_{ik}}{\partial \epsilon_{lm}} \ . \tag{7.3}$$

Since both K_{ik} and ϵ_{lm} are second-rank symmetric tensors, they satisfy $K_{ik} = K_{ki}$ and $\epsilon_{lm} = \epsilon_{ml}$ and thus several symmetry relationships for K_{iklm} follow, such as:

$$K_{iklm} = K_{kilm} = K_{kiml} = K_{ikml} \ , \quad \text{and} \quad K_{iklm} = K_{lmik} \ . \tag{7.4}$$

Here the latter condition comes from the fact that this fourth-rank tensor is symmetric for the interchange of two sets of two indices (ik) and (lm).

6) The rotation of a second-rank tensor is given by: $\begin{pmatrix} \cos\theta & \sin\theta \\ -\sin\theta & \cos\theta \end{pmatrix}\begin{pmatrix} \epsilon_{tt} & 0 \\ 0 & \epsilon_{\ell\ell} \end{pmatrix}\begin{pmatrix} \cos\theta & -\sin\theta \\ \sin\theta & \cos\theta \end{pmatrix}$.

7) The reason why the other K_{iklm} components vanish is given by the condition that the tensor K_{iklm} should be invariant under a $2\pi/3$ rotation. In three dimensions, we should add K_{3333}, K_{1133} and K_{3232} and we then get five different force constants. For the combined index (ij) used to define K_{ij}, we use the notation $(11) = 1$, $(22) = 2$, $(33) = 3$, $(32) = 4$, $(13) = 5$, $(21) = 6$. In this notation, the five independent K_{iklm} components are expressed as: $K_{1111} = K_{11}$, $K_{1122} = K_{12}$, $K_{3333} = K_{33}$, $K_{1133} = K_{13}$, and $K_{3232} = K_{44}$.

Further, the hexagonal symmetry restricts the number of independent components of K_{iklm} to a few, namely, K_{1111} and K_{1122} in the two-dimensional motion and there are three different nonzero values that can be expressed in terms of these two components, namely $K_{1111} = K_{2222}$, K_{1122}, and $K_{1212} = (K_{1111} - K_{1122})/2$ in this case [232]. It is noted that K_{1212} is not independent of K_{1111} and K_{1122} and is expressed as $K_{1212} = (K_{1111} - K_{1122})/2$. By defining the following $\tilde{K}$, the motion of the atoms 1 and 2 in the graphene unit cell is well-characterized by the following definitions:

$$\begin{aligned} M\tilde{K}_{11} &\equiv K_{1111} = K_{2222} \\ M\tilde{K}_{12} &\equiv K_{1122} = K_{2211} \\ \frac{1}{2}M\left(\tilde{K}_{11} - \tilde{K}_{12}\right) &\equiv K_{1212} = K_{2112} = K_{1221} = K_{2121} \,. \end{aligned} \tag{7.5}$$

Then Eq. (7.1) becomes as follows:

$$\begin{pmatrix} \Lambda - (\tilde{K}_{11}\epsilon_{11} + \tilde{K}_{12}\epsilon_{22}) & -(\tilde{K}_{11} - \tilde{K}_{12})\epsilon_{12} \\ -(\tilde{K}_{11} - \tilde{K}_{12})\epsilon_{12} & \Lambda - (\tilde{K}_{11}\epsilon_{22} + \tilde{K}_{12}\epsilon_{11}) \end{pmatrix} \begin{pmatrix} u_1 \\ u_2 \end{pmatrix} = \begin{pmatrix} 0 \\ 0 \end{pmatrix} \,, \tag{7.6}$$

where $\Lambda = \omega^2 - \omega_0^2$ and ϵ_{ij} is expressed by Eq. (7.2). In order to get the solution of $(u_1, u_2)^t \neq (0,0)^t$ (i. e., a nontrivial solution), the determinant of the matrix of Eq. (7.6) should be zero, and this equation is known as the secular equation.

When we put Eq. (7.2) into Eq. (7.6), we get the frequency change $\delta\omega \equiv \omega - \omega_0$ due to strain as follows:[8)]

$$\frac{\delta\omega}{\omega_0} = \frac{\tilde{K}_{11} + \tilde{K}_{12}}{4\omega_0^2}(\epsilon_{\ell\ell} + \epsilon_{tt}) \pm \frac{\tilde{K}_{11} - \tilde{K}_{12}}{4\omega_0^2}(\epsilon_{\ell\ell} - \epsilon_{tt}) \,. \tag{7.7}$$

The hydrostatic component of the strain is defined by

$$\epsilon_h = \epsilon_{\ell\ell} + \epsilon_{tt} \tag{7.8}$$

and the shear component by

$$\epsilon_s = \epsilon_{\ell\ell} - \epsilon_{tt} \,. \tag{7.9}$$

The coefficient to ϵ_h in Eq. (7.7) is the Grüneisen parameter λ:

$$\lambda = -\frac{1}{\omega_0}\frac{\partial\omega}{\partial\epsilon_h} = \frac{\tilde{K}_{11} + \tilde{K}_{12}}{4\omega_0^2} \,, \tag{7.10}$$

which describes the shift in frequency for a hydrostatic deformation (strictly speaking, the deformation is hydrostatic when $\epsilon_{\ell\ell} = \epsilon_{tt}$). The coefficient to ϵ_s in Eq. (7.7) is:

$$\beta = \frac{1}{\omega_0}\frac{\partial\omega}{\partial\epsilon_s} = \frac{\tilde{K}_{11} + \tilde{K}_{12}}{4\omega_0^2} \,, \tag{7.11}$$

8) Here we use the fact that $m(\omega^2 - \omega_0^2) = m(\omega + \omega_0)(\omega - \omega_0) \sim 2\omega_0\delta\omega$. All the $\sin\theta$ and $\cos\theta$ terms in Eq. (7.2) disappear after a long calculation. The reason why this disappearance of $\sin\theta$ and $\cos\theta$ terms occurs is that the graphene system is isotropic in plane.

which describes the shift in frequency for shear stress. For a uniaxial strain, $\epsilon_{\ell\ell}$ and ϵ_{tt} are related by the Poisson ratio, defined as:

$$\nu = (\delta w/w)/(\delta l/l)\,, \tag{7.12}$$

where l and w are, respectively, the length and width of a sheet being deformed along length l. First principles calculations give $\epsilon_{tt} = -0.186\epsilon_{\ell\ell}$ for a graphene sheet [231].

7.1.2
Application of Strain to Graphene

Figure 7.1 shows the evolution of the G-band spectra for a graphene sheet subjected to uniaxial strain [231]. Strain (see Figure 7.1a) causes the G-band to split into two peaks, here named G^+ and G^- (see Figure 7.1d). These bands are related to the longitudinal (G^-) and transverse (G^+) atomic motions with respect to the strain direction (where the eigenvectors are defined in Figure 7.1b,c). The labels iTO and LO as used here have no relation to the concept of iLO and iTO in the graphene phonon dispersion relations, where the modes are longitudinal and transverse with respect to a given phonon modulation direction $\boldsymbol{q}$. A clear picture about the phonon eigenvectors is obtained by considering the dependence of the G-band mode intensities as a function of the light polarization direction (see [198, 230, 231]).

In Figure 7.2, the measured values for the strain-dependent shifts are $\partial\omega_{G^+}/\partial\epsilon = -10.8\,\mathrm{cm}^{-1}/\%$ strain and $\partial\omega_{G^-}/\partial\epsilon = -31.7\,\mathrm{cm}^{-1}/\%$ strain. However, these values vary from one research group to another by a factor of ~ 5 [198, 230, 231], mainly due to the difficulty in performing the experiment accurately. Sample preparation and inhomogeneous bending of the sample are examples of experimental difficulties.

Having the G-band frequency shifts from Figure 7.2, one can use Eq. (7.7) by substituting $\epsilon_{tt} = 0$ and $\epsilon_{ll} = \epsilon$ to obtain the coefficients given in Eqs. (7.10) and (7.11) as

$$\lambda = \frac{\delta\omega_{G^+} + \delta\omega_{G^-}}{2\omega_0(1-\nu)\epsilon} \tag{7.13}$$

$$\beta = \frac{\delta\omega_{G^+} - \delta\omega_{G^-}}{\omega_0(1+\nu)\epsilon}. \tag{7.14}$$

7.2
The G-band in Nanotubes: Curvature Effects on the Totally Symmetric Phonons

The G-band appears as multiple peaks in a SWNT, while a single peak ($\omega_G \approx 1582\,\mathrm{cm}^{-1}$) is observed for a 2D graphene sheet [112, 233]. Up to six G-band phonons are first-order Raman allowed in chiral SWNTs, although two of them (the totally symmetric A_1 modes, see Figure 6.8) usually dominate the spectra. In this section we discuss the effects of curvature in the A_1 symmetry modes.

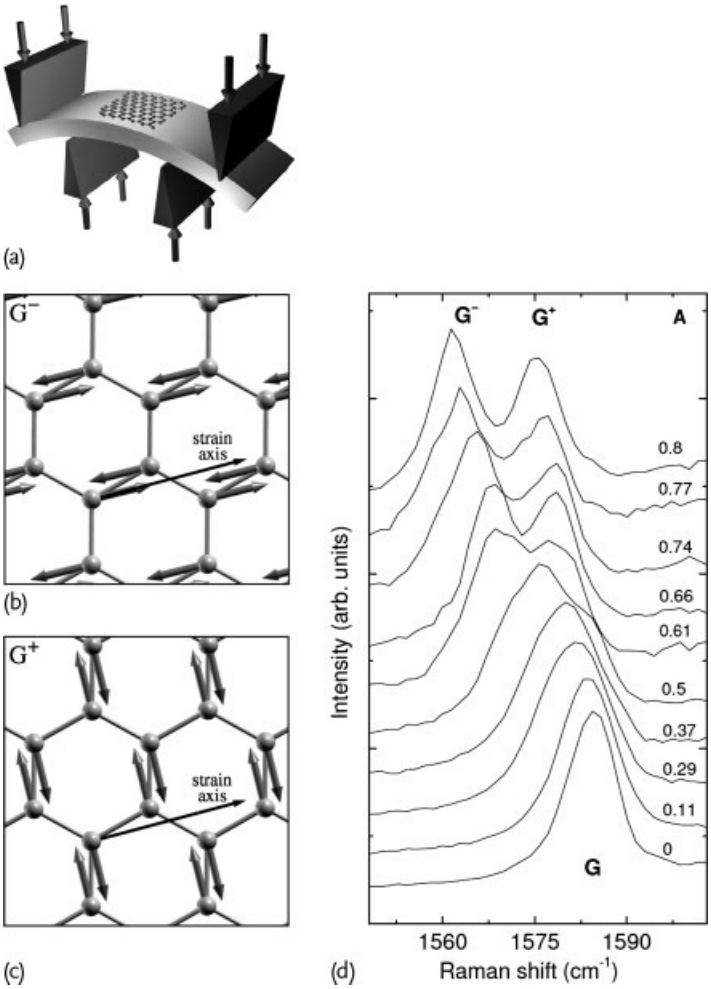

Figure 7.1 The effect of uniaxial strain on graphene. (a) The graphene sheet is deposited on a polymer coated substrate that is bent using the four indicated point supports. (b,c) Eigenfunctions for G^+ (b) and G^- (c) are shown and are determined by density-functional perturbation theory. The direction of the strain axis is indicated for both cases. (d) The G-band spectra thus measured for many values of the applied strain show a splitting into two components, G^+ and G^- that are clearly seen with increasing strain. Note that each spectrum is labeled by its value of the applied strain. Adapted from [231].

7.2.1 The Eigenvectors

In carbon nanotubes, strain exists independent of any external applied force because of nanotube curvature. The system is one-dimensional, so that a longitudinal vibration means atomic motion along the tube axis and a transverse vibration

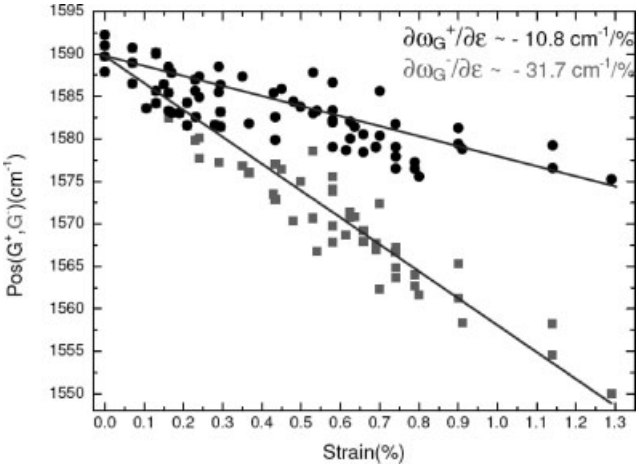

Figure 7.2 G-band frequencies ω_{G+} and ω_{G-} for graphene are plotted as a function of applied uniaxial strain. The solid lines are linear fits to the data, and values for the fitted slopes are indicated for both ω_{G+} and ω_{G-}. Adapted from [231].

means atomic motion perpendicular to the tube axis [234]. *Ab initio* calculations have been performed for (6,6) and (10,0) achiral and (8,4) and (9,3) chiral nanotubes [234]. The authors found that, for achiral (armchair and zigzag) SWNTs, the strict LO and iTO designations of the G-band phonons remain valid. For chiral nanotubes, however, the phonon eigenvectors lie along different directions relative to the nanotube axis, so that we cannot define strict LO and iTO modes by using the nanotube axis direction. In Figure 7.3a we show the A_1 mode displacements for an (8,4) tube and in Figure 7.3b we show the corresponding displacements for a (9,3) M-SWNT [234]. In Figure 7.3 it can be seen that the displacement of the atoms is along the circumference in the (8,4) S-SWNT, but parallel to the bonds in the (9,3) nanotube, thus showing evidence for sensitive dependence of the atomic displacements on the chiral angle. The smallest angle between the carbon-carbon bonds and the circumference in the (9,3) tube is $30^\circ - \theta = 16.1^\circ$ [234].

Of course the θ result is model-dependent and, therefore, despite the importance and the large number of prior works devoted to Raman scattering in SWNTs [112, 233], there is still controversy about whether the many peaks within this G-band can be assigned to (quasi) LO and iTO type mode behavior. There is also controversy about which features pertain to the three different symmetry types (A_1, E_1 and E_2) related to phonon confinement within the first-order *single resonance* process [112, 227, 233], or if all features belong to a totally symmetric irreducible representation (A_1 symmetry) [235, 236] and originate from a defect-induced *double resonance* Raman scattering process [237]. Phonon confinement will be discussed here in Section 7.3.1, while the double resonance process in this connection will be discussed in Chapters 12 and 13, where we then revisit the double-resonance G-band model. For the moment, we consider only the A_1 symmetry modes with iTO and LO character, for simplicity.

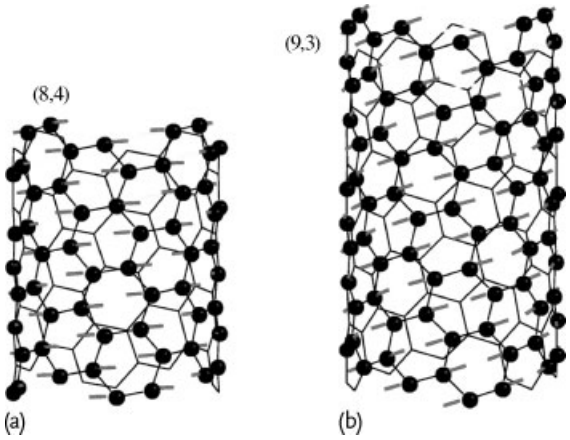

Figure 7.3 (a) The A_1 symmetry high-energy eigenvectors for an (8,4) S-SWNT. The atomic displacements are parallel to the circumference. (b) An A_1 symmetry high-energy eigenvector for a (9,3) M-SWNT. The atomic displacements are parallel to the carbon–carbon bonds. The direction of the helix is indicated by the gray lines [234].

7.2.2
Frequency Dependence on Tube Diameter

The most evident consequence of the strain induced by tube curvature is the ω_G dependence on tube diameter (d_t). Such a dependence has already been introduced in Chapter 4. In Figure 4.12, the filled bullets stand for ω_G from semiconducting SWNTs and the open bullets stand for ω_G from metallic SWNTs. The two most intense A_1 symmetry G peaks, named G^+ and G^- for the higher and lower frequencies, respectively, exhibit the following diameter dependence [179]:

$$\omega_G = 1591 + C/d_t^2 \,, \tag{7.15}$$

where $C_{G+} = 0$, $C_{G-}^S = 47.7\,\mathrm{cm}^{-1}\mathrm{nm}^2$, $C_{G-}^M = 79.5\,\mathrm{cm}^{-1}\,\mathrm{nm}^2$ gives the solid, long dashed and dashed lines in Figure 4.12c, respectively, for semiconducting and metallic SWNTs. Such a dependence is explained as follows. In the time-independent perturbation picture, the ω_G^{LO} mode frequency is expected to be independent of diameter, since the atomic vibrations are along the tube axis. In contrast, the ω_G^{iTO} mode has atomic vibrations along the tube circumference, and increasing the curvature increases the out-of-plane component, thus decreasing the spring constant with a $1/d_t^2$ dependence. This picture holds for S-SWNTs, where G^+ stands for the LO mode, and G^- stands for the iTO mode [179]. However, for M-SWNTs the picture is different: G^+ stands for the iTO mode, and G^- stands for the LO mode [124]. The G-band profile in this case is very different, as shown in the bottom spectrum of Figure 4.12a, and this behavior can only be understood within a time-dependent perturbation picture. This issue is discussed further in Chapter 8.

7.3
The Six G-band Phonons: Confinement Effect

In Section 7.2, we neglected the fact that when rolling up the graphene sheet to form a nanotube, the confinement along the circumferential direction generates a larger number of first-order Raman-active modes. In Section 7.3.1 we discuss mode symmetry and selection rules while in Section 7.3.2 we show how polarization analysis can be used to study the G-band in more depth. For a detailed discussion of the selection rules for the first-order single-resonance Raman scattering process in nanotubes, we direct the reader to Chapter 6.

7.3.1
Mode Symmetries and Selection Rules in Carbon Nanotubes

The A_1, E_1 and E_2 symmetry Raman modes exhibiting zero, two and four nodes along the tube circumference (see Figure 6.8) become Raman-active in SWNTs. These modes are represented using the zone-folding picture in Figure 7.4b. Considering these three symmetries combined with their LO and iTO vibrational nature (displayed in Figure 7.4a), six G-band phonons can be Raman-active in chiral SWNTs (achiral have higher symmetry and only three G-band modes are Raman active). However, their observation depends on the direction of light polarization and on the resonance condition, as discussed below.

Here we select the Z and Y axes as the SWNT axis direction and the photon propagation direction, respectively. Thus we have two independent polarization directions of light, namely parallel (Z) and perpendicular (X) to the nanotube axis. Hereafter we denote a scattering event with incident polarization i and scattered polarization s as (is).[9] Thus we have four different kinds of scattering events: XX,

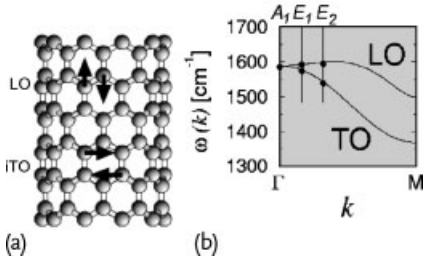

Figure 7.4 (a) Schematic picture of the G-band atomic vibrations along the nanotube circumference and along the nanotube axis of a zigzag nanotube. (b) The Raman-active modes with A_1, E_1, and E_2 symmetries and the corresponding cutting lines $\mu = 0$, $\mu = \pm 1$, and $\mu = \pm 2$ in the unfolded 2D Brillouin zone. The Γ points of the cutting lines are shown by solid dots [80].

9) A more complete notation is $p_i(is)p_s$, named Porto's notation in memory of S.P.S. Porto, where p_i and p_s give the propagation directions for the incident and scattered photons, respectively. Since we only discuss backscattering here, for economy of space we do not use the full notation for the scattering geometry.

Table 7.1 Selection rules for polarization-dependent G-band features and the corresponding resonance conditions. The Z and Y axes are the SWNT axis direction and the photon propagation direction, respectively. The polarization of the incident and scattered light are given as well as the resonance condition. E_G is the G-band phonon energy [226, 227].

Symmetry of phonon	Scattering event	Resonance
A_1	(ZZ)	$E_{laser} = E_{ii}$, $E_{laser} \pm E_G = E_{ii}$
A_1	(XX)	$E_{laser} = E_{ii\pm1}$, $E_{laser} \pm E_G = E_{ii\pm1}$
E_1	(XZ)	$E_{laser} = E_{ii\pm1}$, $E_{laser} \pm E_G = E_{ii}$
E_1	(ZX)	$E_{laser} = E_{ii}$, $E_{laser} \pm E_G = E_{ii\pm1}$
E_2	(XX)	$E_{laser} = E_{ii\pm1}$, $E_{laser} \pm E_G = E_{ii\pm1}$

XZ, ZX and ZZ. Considering the general case of chiral SWNTs (with C_N symmetry) [226, 227], the first-order Raman signal from isolated SWNTs can only be seen when the excitation laser energy is in resonance with a van Hove singularity (VHS). These selection rules imply that, for isolated SWNTs: (1) A_1 symmetry phonon modes can be observed for the (ZZ) scattering geometry when either the incident or the scattered photon is in resonance with E_{ii}, and for the (XX) scattering geometry when either the incident or the scattered photon is in resonance with $E_{i,i\pm1}$. (2) E_1 symmetry modes can be observed for the (ZX) scattering geometry for resonance of the incident photon with E_{ii} VHSs, or for resonance of the scattered photon with $E_{i,i\pm1}$ VHSs, while for the (XZ) scattering geometry for resonance of the incident photon with $E_{i,i\pm1}$ VHSs, or for resonance of the scattered photon with E_{ii} VHSs. (3) E_2 symmetry phonon modes can only be observed for the (XX) scattering geometry for resonance with $E_{i,i\pm1}$ VHSs. Therefore, depending on the polarization scattering geometry and resonance conditions, it is possible to observe 2, 4 or 6 G-band peaks. A summary of the polarization dependence and the corresponding resonance conditions is listed in Table 7.1.

7.3.2 Experimental Observation Through Polarization Analysis

First of all, there is a general and simple polarization behavior that one should bear in mind when acquiring the Raman spectra from a sample of aligned SWNTs, which is not accounted for in the selection rules described in Section 7.3.1. Carbon nanotubes behave as antennas, with the absorption/emission of light being highly suppressed for light polarized perpendicular to the nanotube axis, because of the depolarization effect [238, 239]. Here the depolarization effect means that photoexcited carriers screen the electric field of the cross-polarized light [238, 239]. Therefore, if one wants to measure Raman spectra from a sample of aligned carbon nanotubes, the largest Raman intensity will generally be observed for light polarized along the tube axes (ZZ), and almost no signal will be observed for cross polarized light [228, 235, 240], as shown in Figure 7.5a. Furthermore, when acquir-

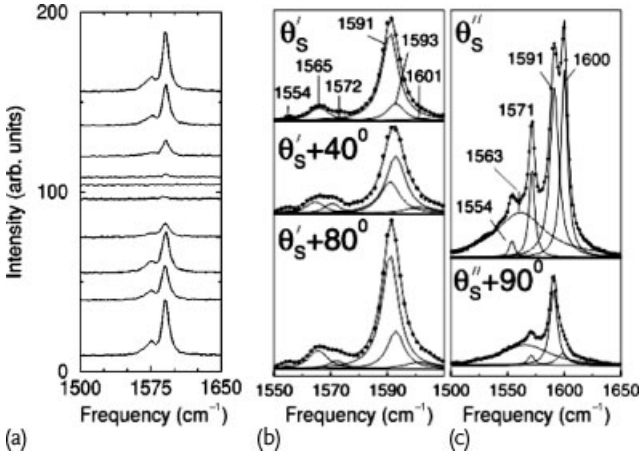

Figure 7.5 (a) Polarization dependence of the G-band from one isolated semiconducting SWNT sitting on a Si/SiO_2 substrate [228]. Both incident and scattered light are polarized parallel to each other and vary from parallel (bottom) to perpendicular (middle) and back to parallel (top) to the tube axis. Parts (b) and (c) show the polarization scattering geometry dependence for the G-band from two isolated SWNTs. The Lorentzian peak frequencies are given in units of cm^{-1}. θ'_S and θ''_S are the incident angles between the light polarization and SWNT axis directions, not known *a priori*. From the relative intensities of the polarization behavior of the G-band modes, $\theta'_S \sim 0°$ and $\theta''_S \sim 90°$ are assigned [226].

ing polarized spectra from a single SWNT with a fixed laser energy, it is not usual to observe Raman signals from both parallel (ZZ) and perpendicular (ZX, XZ, XX) polarization, since the resonance energies for the polarized light in different polarization directions are different from each other (see Table 7.1). This combination of properties make the totally symmetric A_1 mode dominant in the G-band spectra.

However, the most interesting results coming from the polarization analysis are related to the symmetry selection rules for the different phonon/electron symmetries [227, 228, 241], as discussed in Section 7.3.1. Figure 7.5b shows three different G-band Raman spectra from an S-SWNT, but with three different directions for the incident light polarization, that is, θ'_S, $\theta'_S + 40°$ and $\theta'_S + 80°$, where θ'_S is an angle between the initial polarization directions of the light and the nanotube axis. Six well-defined peaks associated with the G-band features are observed, with different relative intensities for the different polarization geometries, and the symmetries of the various peaks are assigned as follows: 1565 and 1591 $\rightarrow$ A_1 symmetry; 1572 and 1593 $\rightarrow$ E_1 symmetry; 1554 and 1601 $\rightarrow$ E_2 symmetry. Figure 7.5c shows two G-band Raman spectra obtained from another S-SWNT ($\omega_{\mathrm{RBM}} = 132\,cm^{-1}$), with θ''_S and $\theta''_S + 90°$. The spectra can be fit using four sharp Lorentzians, and a broad feature at about $1563\,cm^{-1}$. This broad feature (FWHM $\sim 50\,cm^{-1}$) is sometimes observed in weakly resonant G-band spectra from S-SWNTs and they are not discussed here.[10] From previous polarization Raman studies [227], the

10) These features are likely generated by the defect-induced double resonance processes, discussed in Section 13.5.

sharp peaks at 1554 and 1600 cm^{-1} should be assigned as E_2 symmetry modes, while the 1571 and 1591 cm^{-1} peaks should be assigned as unresolved ($A_1 + E_1$) symmetry modes, their relative intensities depending on the incident light polarization direction [227].

It is interesting to note the relatively high intensity of the spectra with (XX) polarization observed in Figure 7.5c, indicating resonance with $E_{i,i\pm1}$ optical transitions. For several measured isolated SWNTs, the Raman intensities in Figure 7.5 do not exhibit a substantial reduction for any direction of the incident/scattered light, in contrast to other published results [228, 235, 240], which showed an intensity ratio $I_{ZZ} : I_{XX} \sim 1 : 0$. From our discussion, it is clear that the so-called antenna effect is observed for samples in resonance with only E_{ii} electronic transitions, and that is the case in Figure 7.5a and [228, 235, 240]. However, in general, the intensity ratio ZZ:XX can assume values either larger or smaller than 1, depending on the resonance condition. The samples in [227] exhibit a very large diameter distribution (d_t from 1.3 nm up to 2.5 nm), so that E_{ii} and $E_{i,i\pm1}$ transitions can both occur within the resonance window of the same laser, and an average value of $ZZ : XX = 1.00 : 0.25$ was then observed.

7.3.3
The Diameter Dependence of ω_G

Now that the phonon confinement has been introduced, a more complete picture for the diameter dependence of the G-band than that introduced in Section 7.2.2 can be given. Figure 7.6 shows the G-band phonon frequencies as a function of tube diameter evaluated by zone folding of the graphene phonon dispersion relations (lines) in comparison to *ab initio* calculations (points) [124]. The diameter dependence of the dispersion relations based on zone folding comes from the diameter dependence of the distance between adjacent cutting lines. A single A_1 mode is predicted since the phonon frequencies of the LO and iTO modes are identical to each other at the Γ point in graphite (see Figure 7.4b). Additionally, zone folding shows a relatively small splitting between the longitudinal and transverse E_1 modes, and a larger splitting between the two E_2 modes. A large mode softening is observed for small diameters as the cutting line reaches the maximum of the phonon dispersion for the LO branch in Figure 7.4b.

The full *ab initio* calculations show a similar behavior, but some details are clearly different. Generally, the *ab initio* results are lower in frequency than the zone-folded values. The frequency softening of the *ab initio* points is explained by the fact that curvature weakens the π contribution to the bonds in the circumferential direction, which also explains why the A_1(T) mode[11] is affected most strongly by curvature, whereas the A_1(L) mode is essentially independent of diameter for semiconducting tubes. For diameters of about 1.4 nm, the E_2 modes (squares at approximately 1613 cm^{-1} and 1570 cm^{-1} in Figure 7.6) are symmetrically split by ± 22 cm^{-1} with respect to the central graphite frequency $\omega_G = 1592$ cm^{-1} (theo-

11) Here, T and L denote the iTO and LO phonon modes, respectively, as adopted in [124].

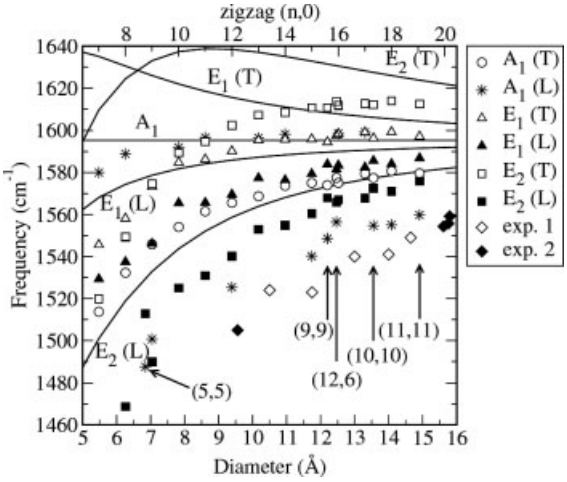

Figure 7.6 Diameter dependence of phonon frequencies of $(n, 0)$ zigzag, (n, n) armchair and (12,6) chiral SWNTs for the G-band calculated by *ab initio* density functional theory (symbols) and by zone folding (lines). Phonons are characterized by their symmetry and whether they are T or L modes. Here L denotes vibration (longitudinal) displacements parallel to the tube axis while T denotes vibrational displacements transverse or perpendicular to the tube axis. The lower axis and upper axis show the diameter and the $(n, 0)$ index scales for zigzag tubes, respectively. [124]

ry). Since the tube curvature shifts the E_1(T) mode to lower values, the frequencies of the E_1(T) and A_1(L) modes (open triangles and asterisks) almost coincide for S-SWNTs and are located at about 1597 cm^{-1}, a little bit higher in frequency than the theoretical central G-band mode of graphite. The E_1(L) and A_1(T) symmetry G-band modes (filled triangles and open circles in Figure 7.6) also have rather similar frequencies and are found at roughly 1580 cm^{-1}, that is, 20 cm^{-1} lower than the E_1(T) and A_1(L) modes. The (n, m) labeled tubes indicate a downshifted $A_1(L)$ for metallic SWNTs, and theseunusual results will be discussed in Chapter 8.

Further confirmation for the G-band mode assignment proposed in Section 7.3.1 comes from comparison of experimental results with *ab initio* calculations. Here we focus on the spectra from semiconducting SWNTs because metallic SWNTs exhibit time-dependent perturbations that will be discussed in Chapter 8. Figure 7.7 plots the G-band mode frequencies for several resonant S-SWNTs vs. the observed ω_{RBM} (bottom axis) and vs. inverse nanotube diameter where the relation $1/d_t = \omega_{\mathrm{RBM}}/248$ was used to label the top axis of Figure 7.7.[12] The spectra are usually fit using 6 peaks, although sometimes only 4 or 2 peaks are used, the spectra beingfit with linewidths approaching the natural linewidth for the G-band modes [242], that is, $\gamma_G \sim 5\,\mathrm{cm}^{-1}$.

12) The $\omega_{\mathrm{RBM}} = 248/d_t$ relation [176] has been broadly used in the early years of single nanotube spectroscopy (2001–2005), although now we know it represents a special case. How to obtain the tube diameter from the SWNT radial breathing mode frequency (ω_{RBM}) is the subject of Chapter 9.

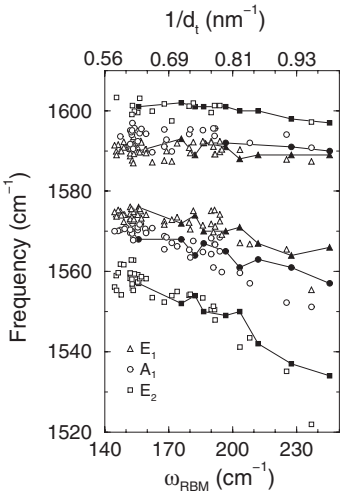

Figure 7.7 Correlation of ω_G and ω_{RBM} shown by plotting ω_G (open symbols) vs. ω_{RBM} (bottom axis) and vs. $1/d_t$ (top axis) for S-SWNTs. Experimental G-band data obtained with $E_{laser} = 1.58$, 2.41 and 2.54 eV. Solid symbols connected by solid lines come from *ab initio* calculations [124] downshifted by 18, 12, 12, 7, 7, 11 cm^{-1} from the bottom to the top of the *ab initio* data, respectively [226].

The solid symbols connected by solid lines in Figure 7.7 come from calculations by Dubay *et al.* (Figure 7.6). The different solid symbols indicate the different mode symmetries: $\bullet \rightarrow A_1$, $\blacktriangle \rightarrow E_1$, $\blacksquare \rightarrow E_2$, in agreement with polarization results (see Figure 7.5). The theoretical points in Figure 7.7 were downshifted by about 1% to fit the experimental data. The observed d_t dependence of the frequencies for each of the 3 higher frequency G^+-band modes (A_1, E_1 and E_2) are in very good agreement with theory [124], showing little d_t dependence. For the 3 lower frequency G^--band modes, both *ab initio* calculations and experimental results show a stronger d_t dependence, but *ab initio* calculations seem to slightly underestimate the G^--band mode softening for lower d_t values (mainly for the A_1 symmetry mode). The experimental data from semiconducting SWNTs can be better fit with [226]

$$\omega_G = 1592 - C/d_t^{\beta}\,, \tag{7.16}$$

with $\beta = 1.4$, $C_{A_1} = 41.4\,cm^{-1}\,nm$, $C_{E_1} = 32.6\,cm^{-1}\,nm$, and $C_{E_2} = 64.6\,cm^{-1}\,nm$.

7.4 Application of Strain to Nanotubes

Different authors have applied externally induced strain to carbon nanotubes, both in bundles [236, 243] and as isolated tubes [244–246]. The elasticity theory presented in Section 7.1.1 is also used to study strain in carbon nanotubes, and it has

actually been initially developed for these cases [232]. Measurements on SWNT bundles basically show an overall increase in ω_G by increasing hydrostatic pressure [236, 243]. This result was initially used as evidence for the absence of LO and iTO G-band mode behavior. However, measurements on isolated tubes show a greater richness of effects, which includes both hydrostatic and uniaxial deformation, torsion, bending, etc. Here a large downshift in the E_2 modes was observed and different pressure-induced effects for G^+ vs. G^- were found, depending on (n, m) [247]. For isolated S-SWNTs with uniaxial strain up to 1.65%, shifts in ω_G of up to $40\,cm^{-1}$ were observed [244]. There are still some controversial results regarding strain effects in SWNTs, mostly because of the difficulty to perform the experiments accurately and the need for a large number of measurements to establish and understand the (n, m) dependence.

7.5 Summary

The stretching of the C–C bond in sp^2 graphitic materials gives rise to the so-called G-band. The G-band is highly sensitive to strain effects in sp^2 nanocarbons, and can be used to probe any modification in the flat geometric structure of graphene, such as the strain that is induced by external forces, or even by the curvature when growing a SWNT. This curvature dependence generates a diameter dependence, thus making the G-band a probe also for the tube diameter, while its dependence on externally induced strain is very rich and still controversial. Phonon confinement in SWNTs generate complex selection rules that can be tested using light polarization analysis, although the antenna effect causes the totally symmetric modes to dominate the spectra most of the time. Finally, the G-band of metallic SWNTs is special, and this comes from electron–phonon coupling that can only be treated within time-dependent perturbation theory. This effect generates interesting results in both graphene and carbon nanotubes, related to both temperature and doping. These issues will be discussed in Chapter 8.

Problems

[7-1] Explain that the Coulomb interaction between positive and negative ions in an ionic crystal changes the force constant for the LO phonon mode but not for the iTO phonon mode.

[7-2] When we consider the frequency-dependent dielectric constant $\epsilon(\omega)$, the ratio of the LO to the iTO phonon frequency in an ionic crystals is given by:

$$\frac{\omega_{LO}}{\omega_{iTO}} = \frac{\epsilon(0)}{\epsilon(\infty)} ,$$

which was derived by Lyddane, Sachs, and Teller (LST theory). Study the LST theory and obtain the above formula. Check that the formula works for some ionic crystals such as NaCl.

[7-3] The above LST relation is considered for $\boldsymbol{q} = 0$. For a general $\boldsymbol{q}$ vector, we can discuss how the phonon dispersion is modified by the Coulomb interaction by considering the coupling of Maxwell's equations to the equation of motions for the atoms:

$$\ddot{\boldsymbol{x}} + \omega_{\mathrm{iTO}}^2 \boldsymbol{x} - a E_x = 0$$

$$P_x = a\boldsymbol{r} + (\epsilon(\infty) - 1) E_x \ ,$$

where a is given by:

$$a = \omega_{\mathrm{iTO}} [\epsilon(0) - \epsilon(\infty)]^{1/2} \ .$$

Combining these two equations with Maxwell's equations for $D_x = E_x + P_x$ and for H_x, and considering their wave vector $\boldsymbol{q}$, obtain and plot $\omega(q)$.

[7-4] When we pull a hexagonal net in one direction, how much percent of the length of the net can be expanded compared with the length of an undistorted hexagonal net. When we rotate the pulling direction relative to the C–C bond direction, how does the expansion ratio change? Compare these results with the case of a square or triangular net.

[7-5] Consider two carbon atoms which are connected to each other by a spring. Evaluate the force constant in units of eV/Å^2 (use the 1580 cm^{-1} LO phonon mode frequency for sp^2 carbons).

[7-6] Consider a $2\pi/3$ rotation around a carbon atom in the plane of graphene. Make a 3 rotation matrix $D(2\pi/3)$ for the $2\pi/3$ rotation around the z axis.

[7-7] Let us consider a function $f = ax + by + cz + d$. When a vector (x, y, z) is transformed by this $2\pi/3$ rotation into $(x', y', z') = D(2\pi/3)(x, y, z)$ and suppose that f is invariant for the $2\pi/3$ rotation, then show $a = b = c = 0$.

[7-8] Let us consider a function $g = ax^2 + by^2 + cz^2 + dyz + ezx + fxy$. When a vector (x, y, z) is transformed by the $2\pi/3$ rotation as $(x', y', z') = D(2\pi/3)(x, y, z)$ and suppose that g is invariant for the $2\pi/3$ rotation, what are the conditions imposed for the constants a, b, c, d, e, f.

[7-9] A second rank tensor can be defined as a 3×3 matrix a_{ij} in which a is transformed by any invariant operation $(x', y', z') = C(x, y, z)$, where C is a matrix that transforms into $a' = C^{-1} a C$. Because the determinant of a should not be changed by C, show that det(C)=1 and that $a_{ij} = a_{ji}$. Thus a symmetric second rank tensor has six independent components.

[7-10] When we consider a fourth-rank tensor K_{iklm} in three dimension $(i, k, l, m = 1, 2, 3)$, 81 possible variables exist. However, because of the

relationship of Eq. (7.4), K_{iklm} has only 21 independent variables even though there is no symmetry for the system. Explain this statement.

[7-11] What is the relationship between the LO and iTO phonon mode frequencies with the Young's modulus and other force constants?

[7-12] In the D_N symmetry, show that only A_1, E_1, and E_2 phonon modes are Raman-active. If we plot the one-dimensional Brillouin zone (cutting lines), which lines in the 2D Brillouin zone correspond to the Raman-active modes? Answer by constructing a figure.

[7-13] Plot the X, Y, Z axes and show the scattering geometries with the corresponding resonance conditions for carbon nanotubes when we put a carbon nanotube with its axis along the Z axis and when the light is coming from the Y (or Z) direction.

[7-14] The curvature of a nanotube is considered to have a constant strain in one direction. Then estimate the change in the iTO and LO phonon frequencies.

[7-15] Show how to obtain Eqs. (7.13) and (7.14) from the definitions in Section 7.1.1.

[7-16] Apply the theory developed in Section 7.1.1 for carbon nanotubes, and obtain the effect of strain on the transverse and longitudinal modes. You can use [232] as a guide.

[7-17] Study the difference between Eqs. (7.15) and (7.16). Can these two equations be consistent?

[7-18] Make a study of the Poisson ratio and the Grüneisen parameter for graphene, graphite and carbon nanotubes.